



Chinese Pharmaceutical Association
Institute of Materia Medica, Chinese Academy of Medical Sciences

Acta Pharmaceutica Sinica B

www.elsevier.com/locate/apsb
www.sciencedirect.com



ORIGINAL ARTICLE

Pulmonary endothelium-targeted nanoassembly of indomethacin and superoxide dismutase relieves lung inflammation



Yi Yang^{a,b,†}, Makhloufi Zoulikha^{a,b,†}, Qingqing Xiao^{b,c,†},
Feifei Huang^b, Qi Jiang^b, Xiaotong Li^b, Zhenfeng Wu^{d,*}, Wei He^{a,b,*}

^aShanghai Skin Disease Hospital, Tongji University School of Medicine, Shanghai 200443, China

^bSchool of Pharmacy, China Pharmaceutical University, Nanjing 2111198, China

^cDepartment of Traditional Chinese Medicine Processing and Preparation, Nanjing University of Chinese Medicine, Nanjing 210023, China

^dKey Laboratory of Modern Preparation of TCM, Ministry of Education, Jiangxi University of Chinese Medicine, Nanchang 330004, China

Received 2 February 2023; received in revised form 5 May 2023; accepted 6 May 2023

KEY WORDS

Codelivery;
Nanocrystals;
Superoxide dismutase;
Indomethacin;
Pulmonary endothelium;
Inflammation;
Acute lung injury

Abstract Lung inflammation is an essential inducer of various diseases and is closely related to pulmonary-endothelium dysfunction. Herein, we propose a pulmonary endothelium-targeted codelivery system of anti-inflammatory indomethacin (IND) and antioxidant superoxide dismutase (SOD) by assembling the biopharmaceutical SOD onto the “vector” of rod-like pure IND crystals, followed by coating with anti-ICAM-1 antibody (Ab) for targeting endothelial cells. The codelivery system has a 237 nm diameter in length and extremely high drug loading of 39% IND and 2.3% SOD. Pharmacokinetics and biodistribution studies demonstrate the extended blood circulation and the strong pulmonary accumulation of the system after intravenous injection in the lipopolysaccharide (LPS)-induced inflammatory murine model. Particularly, the system allows a robust capacity to target pulmonary endothelium mostly due to the rod-shape and Ab coating effect. *In vitro*, the preparation shows the synergistic anti-inflammatory and antioxidant effects in LPS-activated endothelial cells. *In vivo*, the preparation exhibits superior pharmacodynamic efficacy revealed by significantly downregulating the inflammatory/oxidative stress markers, such as TNF- α , IL-6, COX-2, and reactive oxygen species (ROS), in the lungs. In

*Corresponding authors.

E-mail addresses: zfwu527@163.com (Zhenfeng Wu), weihe@cpu.edu.cn (Wei He).

[†]These authors made equal contributions to this work.

Peer review under responsibility of Chinese Pharmaceutical Association and Institute of Materia Medica, Chinese Academy of Medical Sciences.

<https://doi.org/10.1016/j.apsb.2023.05.024>

2211-3835 © 2023 Chinese Pharmaceutical Association and Institute of Materia Medica, Chinese Academy of Medical Sciences. Production and hosting by Elsevier B.V. This is an open access article under the CC BY-NC-ND license (<http://creativecommons.org/licenses/by-nc-nd/4.0/>).

conclusion, the codelivery system based on rod-like pure crystals could well target the pulmonary endothelium and effectively alleviate lung inflammation. The study offers a promising approach to combat pulmonary endothelium-associated diseases.

© 2023 Chinese Pharmaceutical Association and Institute of Materia Medica, Chinese Academy of Medical Sciences. Production and hosting by Elsevier B.V. This is an open access article under the CC BY-NC-ND license (<http://creativecommons.org/licenses/by-nc-nd/4.0/>).

1. Introduction

Lung inflammation is an underrecognized risk for various diseases such as cardiovascular disease, acute lung injury (ALI), and pulmonary hypertension¹. ALI represents a serious lung inflammation disease that may progress to acute respiratory distress syndrome (ARDS), pulmonary fibrosis, and even severe systemic complications, as currently seen in coronavirus disease 2019 (COVID-19)^{2,3}. Due to the high mortality rate of over 30%–40%, ALI has always been a difficult point in scientific research and clinical practice^{4–6}. So far, the clinical practices against ALI/ARDS are mainly symptomatic, including protective ventilation and fluid management, but no specific therapy based on the pathophysiological attributes of the disorder is available^{7,8}. Regardless of the triggering factors of ALI (pneumonia, sepsis, trauma, multiple transfusions, etc.), the terminal pathophysiological features are similar, including dysregulated inflammatory response and defective alveolar clearance leading to pulmonary edema, impaired gas exchange, and hypoxemia⁹.

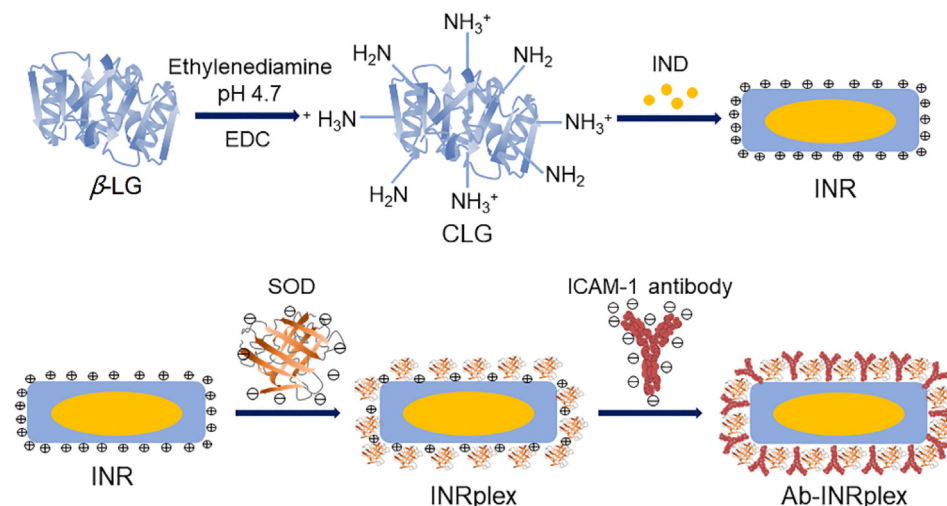
Pulmonary vascular injury is an important pathological hallmark of ALI/ARDS¹⁰. The lung endothelium is highly vulnerable to direct and indirect ALI triggers causing functional and structural alterations of endothelial cells¹⁰. Also, the pulmonary endothelial cells can be directly activated by endotoxins attachment, activating the transcription of nuclear factor kappa B (NF- κ B)-dependent proinflammatory genes. The injured pulmonary endothelium exacerbates the inflammatory response by secreting proinflammatory factors, producing reactive oxygen species (ROS) such as the superoxide anion and hydroxyl radical, and facilitating leukocytes migration to the injury site by the overexpression of adhesion molecules^{11–13}. For example, the overproduced proinflammatory cytokines such as interleukins and tumor necrosis factors (TNF- α) lead to the recruitment of inflammatory cells such as macrophages and neutrophils to the lungs that produce more proinflammatory mediators and ROS^{2,9,14–16}. Meanwhile, ROS upregulates the expression of proinflammatory cytokines through inflammasome pathways and consequently intensifies inflammation^{17–20}. Therefore, pulmonary-endothelium targeting for inflammation alleviation seems promising to fight against ALI.

Indomethacin (IND) and superoxide dismutase (SOD) are anti-inflammatory and antioxidant drugs, respectively. IND is a non-steroidal anti-inflammatory drug that attenuates inflammation by targeting inducible cyclooxygenase-2 (COX-2), converting arachidonic acid released from the phospholipids of damaged cell membranes into proinflammatory prostaglandins, such as prostaglandin E2 (PGE2), and strengthening the expression of NF- κ B and the synthesis of cytokines in a positive feedback loop^{21–23}. Meanwhile, COX-2 inhibition could lessen lung inflammation and the production of proinflammatory chemokines in animal models of lung injury^{24,25}. More interestingly, IND was widely proposed

against the infection inflammation induced by SARS-CoV-2^{26–29}, mainly due to its safety. As of 21 January 2023, two recruiting clinical trials testing the efficacy of IND in COVID-19 were registered in the public domain ([ClinicalTrials.gov](https://clinicaltrials.gov) Identifiers: NCT05007522 and NCT04344457). SOD is a potent antioxidant enzyme that can convert intracellular ROS into oxygen and water and inhibit endothelial proinflammatory activation. The enzyme demonstrates higher activities and lower immunogenicity and is administered with a significantly lower dose than other antioxidants^{19,30}. As a result, targeted codelivery of IND and SOD to the pulmonary endothelium can potentially relieve serious lung inflammation.

However, the two drugs possess different physicochemical properties, making their codelivery challenging. The small molecule IND is poorly water-soluble, whereas the biological drug SOD has a molecular weight of 32.5 kDa and high water-solubility³¹. Furthermore, the exogenously administered SOD has a short half-life due to its *in vivo* instability and rapid renal excretion. Invariably, the enzyme displays poor membrane penetration and cellular uptake and little ability to target the inflamed sites^{32,33}. Drug delivery systems (DDS) with tunable size and surface properties can be exploited to load different therapeutic agents to improve their physicochemical properties, protect them from degradation in the bloodstream, control their release, optimize their pharmacokinetic profiles, and effectively deliver them to the diseased area^{34–36}. Various nanosized DDS, such as polymeric and lipid nanoparticles, have been employed to promote drug delivery to the lungs and pulmonary vessels³⁷. However, these traditional DDSs are often spherical and demonstrate a limited ability to deliver the payloads to the pulmonary endothelium due to low drug-loading capability and inadequate endothelium-contact area^{38,39}. In contrast, rod-like nanoparticles with particular aspect ratios favor lung distribution and accumulate at the vascular wall after intravenous injection^{38,40}. Interestingly, several nanocrystals of insoluble drugs, which are pure drug nanoparticles with almost 100% drug loading, usually have rod-like shapes, such as IND, paclitaxel, lovastatin, and baicalein nanocrystals^{41–46}. Therefore, we expected that the rod-shaped IND nanocrystals, termed IND nanorods (INRs), could target the pulmonary endothelium.

In this study, INRs were utilized as a “vector” and assembled with the antioxidant SOD through electrostatic interaction, followed by coating with anti-ICAM-1 antibody (Ab) for targeting intracellular adhesion molecule-1 (ICAM-1) on endothelial cells (Scheme 1). The targeted codelivery system was developed to specifically codeliver the anti-inflammatory IND and the antioxidant SOD to the dysfunctional pulmonary endothelium and alleviate the inflammatory/oxidative profiles of the severe lung inflammation disease, ALI. To obtain proof-of-concept, we performed various experiments *in vitro* and *in vivo*, including preparation and characterization, cellular trafficking, synergistic effect,



Scheme 1 Schematic illustration of Ab-INRplex preparation. First, β lactoglobulin (β -LG) and 1-ethyl-3-(3-dimethylpropylamine) carbodiimide (EDC) were mixed with ethylenediamine at pH 4.7 to prepare cationic lactoglobulin (CLG). Second, INRs were prepared by antisolvent precipitation followed by ultrasonication using CLG as a stabilizer. Finally, Ab-INRplex was fabricated by absorbing SOD onto NRs *via* electrostatic interaction, followed by ICAM-1 antibody incubation.

pharmacokinetics, biodistribution, pulmonary-endothelium targeting, and *in vivo* efficacy against the LPS-induced ALI mice model.

2. Materials and methods

2.1. Materials

IND (I7378), β -LG (L3908), and LPS (L2880) were obtained from Sigma–Aldrich (MO, USA). Cationic β -lactoglobulin (CLG) was synthesized *via* conjugation of ethylenediamine to β -lactoglobulin (β -LG) as described in our previous report^{47,48}. Anti-ICAM-1 antibody (15364-1-AP) were obtained from proteintech Group, Inc. (Chicago, IL, USA). SOD (ml063052) and COX-2 (ml062904) ELISA kits were procured from Shanghai Enzyme-linked Biotechnology (Shanghai, China). TNF- α (SCA133Mu) and IL-6 (SEA079Mu) ELISA kits were purchased from Cloud-Clone Corp (Wuhan, China). The total SOD activity test kit (S0109-2, NBT method) and Lyso-Tracker Red (C1046) were purchased from (Beyotime Biotechnology, Shanghai, China). All other used chemicals were of analytical grade.

2.2. Cell culture and animals

Human umbilical vein endothelial cells (HUVECs) were cultured in an endothelial cell-specific medium (ECM, U.S. Sciencell Research Laboratories) supplemented with 5% fetal bovine serum (FBS), 1% endothelial cell growth factor, and 100 U/mL penicillin + 100 μ g/mL streptomycin at 37 °C in a 5% CO₂ humidified incubator.

All experimental protocols were carried out following the principles of Laboratory Animal Care and the Guide for the Care and Use of Laboratory Animals and approved by the China Pharmaceutical University Institutional Animal Care and Use Committee. ALI mouse model was established 4 h after

intravenous injection of LPS at a dose of 0.8 mg/kg into male BALB/c mice (6–8-week-old, weighting 20–25 g).

2.3. Preparation of INRs, INRplex and Ab-INRplex

First, the INRs were prepared by antisolvent precipitation followed by ultrasonication using cationic β -LG (CLG) as a stabilizer, according to our previous report⁴⁴. Different amounts of IND were dissolved in 0.4 mL of acetone and added dropwise to 10 mL of CLG (1 mg/mL) aqueous solution. Then, the suspension was ultrasonicated in an ice bath (4 °C). The organic solvent was removed by rotary evaporation under reduced pressure to obtain INRs.

Next, INR/SOD complex (INRplex) was obtained by electrostatic interaction between the negatively charged SOD and the positively charged INRs. SOD aqueous solutions with different concentrations were incubated with an equal volume of INR solution (CLG concentration of 1 mg/mL) for 30 min at room temperature to obtain INRplex. Finally, INRplex was mixed with an anti-ICAM-1 solution to allow the antibodies to attach to the residual positive charges of INRplex to obtain Ab-INRplex. The number of antibodies conjugated to the surfaces of INRplex was quantified using the BCA assay. The antibodies were added to the INRplex at a ratio of 15, 30, 60, and 120 μ g of antibodies per 1 mg of NPs. The dye-labeled nanoparticles were prepared similarly but by dissolving FITC (fluorescein isothiocyanate isomer) or DiR (dioctadecyl-tetramethyl indotricarbocyanine iodide) with IND or using RITC (rhodamine B isothiocyanate)-labeled SOD instead SOD.

2.4. Characterization of the nanoparticles

The particle size, polydispersity index (PDI), and zeta potential of the nanoparticles were measured with a 90Plus ZetaPlus Zeta Potential Analyzer (Brookhaven Instruments, Holtsville, NY) at 25 °C. The morphology of nanoparticles was examined using a

JEM-1230 transmission electron microscope (TEM, Tokyo, Japan). The prepared nanoparticles with 200-fold dilution were placed on a copper mesh TEM grid for 10 min, and then the excess liquid was removed with filter paper, followed by adding one drop of 2% (w/w) phosphotungstic acid for 1 min to stain the nanoparticles. Then, the sample was dried at 25 °C.

Gel electrophoresis assay was used to assess the loading of SOD onto INRs. INRplex with CLG:SOD mass ratios of 1:1, 2:1, 4:1, 8:1, 16:1, 32:1, and 64:1 were prepared. Free SOD was used as a control. Electrophoresis was carried out at 30 mA for 1 h, and finally, the gel was transferred to Coomassie brilliant blue solution for overnight staining.

For the investigation of interactions between IND and CLG, INRs with different IND loadings were prepared and scanned with a fluorescence spectrophotometer (Shimadzu RF-5301 PC, Japan) using the excitation wavelength of 295 nm and the emission wavelength range of 300–800 nm. The same samples were analyzed with circular dichroism (CD) to further confirm the combination between CLG and IND using the following parameters: wavelength range, 250–190 nm; bandwidth, 1 nm; scanning speed, 100 nm/min; cell length, 0.1 cm; response, 1 s; temperature, 25 °C; protein concentration, 0.1 mg/mL.

Powder X-Ray diffraction (PXRD) analysis was conducted on a D8 advanced diffractometer (Bruker, Germany). The scanning range was 3–40° (2 θ) at a speed of 1°/min. The pattern was collected at a 40 kV tube voltage and 40 mA of tube current in step scan mode (step size 0.02°, counting time 1 s/step).

For the serum-stability study, the nanoparticles were incubated in PBS containing 10% serum at 37 °C, followed by measuring the particle size and PDI at different time points.

2.5. Drug loading and encapsulation efficiency

The nanoparticles were centrifuged at 5000 \times g for 20 min (TDZ5-WS, Cence, Hunan Xiangyi Instrument Co., Ltd.). The IND content was determined in the supernatant by high-performance liquid chromatography (HPLC, SHIMAZU LC-10AT, Kyoto, Japan) using an ODS C18 column (250 mm \times 4.6 mm, 5 μ m, Diamonsil, Beijing, China) at 40 °C, 0.1 mol/L glacial acetic acid solution-acetonitrile (50/50, v/v) as mobile phase at a flow rate of 1 mL/min and injection volume of 40 μ L. The detection was made at 288 nm. For SOD determination, RITC-Ab-INRplex prepared using RITC-labeled SOD were centrifuged at 5000 \times g for 20 min. Then, the fluorescence intensity of the supernatant was measured using a fluorescence microplate reader (POLARstar, Omega, Germany). The drug loading (DL) and encapsulation efficiency (EE) was calculated according to the following Eqs. (1) and (2):

$$\text{DL (\%)} = \frac{\text{The amount of encapsulated drug}}{\text{The amount of added drug} + \text{The amount of carrier}} \times 100 \quad (1)$$

$$\text{EE (\%)} = \frac{\text{The amount of encapsulated drug}}{\text{The amount of added drug}} \times 100 \quad (2)$$

2.6. In vitro drug release

The *in vitro* release behavior of IND and SOD from Ab-INRplex at pH 7.4 and 6.8 was investigated by the dialysis method. Ab-INRplex and RITC-Ab-INRplex prepared using RITC-labeled SOD were placed into dialysis bags with MWCO of 3500 Da and 100 kDa, respectively, and shaken in a water bath (100 rpm/min) at 37 °C. At predetermined time intervals, 1 mL of the release

medium (PBS) was withdrawn and replaced with an equal volume of fresh release medium. The content of IND and SOD in the release medium was determined as described in the previous section. Simultaneously, the activity of the released SOD at each time point was measured using the total SOD activity test kit (NBT method, Beyotime Biotechnology, Shanghai, China) following the manufacturer's instructions.

2.7. Cell viability

The cytotoxicity of the optimized formulation on HUVECs and PSMCs was measured using the 3-(4,5-dimethylthiazol-2-yl)-2,5-diphenyltetrazolium bromide (MTT) assay. The cells were seeded in 96-well plates at a density of 5×10^3 cells/well for 48 h and incubated with preparations containing different drug concentrations for 48 h at 37 °C.

2.8. Confocal laser scanning microscopy

Confocal laser scanning microscopy (CLSM, LSM 800, Carl Zeiss, Jena, Germany) was used to qualitatively evaluate the expression of ICAM-1 on the surface of HUVECs. The cells (1×10^5 cells/mL) were seeded on glass-bottom culture dishes and incubated for 24 h at 37 °C. Then, HUVECs were activated with LPS (2.5 μ g/mL) for 2 h, washed 3 times with PBS, treated with ICAM-1 primary antibody (1:100) overnight at 4 °C, washed 3 times with PBS and incubated with CoraLite 594 fluorescently labeled secondary antibodies (1:1000) for 1 h at 37 °C in the dark. Finally, the cells were stained with DAPI for 15 min and observed under CLSM. Similarly, the qualitative study of nanoparticle uptake was performed using CLSM. HUVECs (1×10^5 cells/mL) were seeded on glass bottom culture dishes and incubated for 24 h at 37 °C. Then, the cells were activated with LPS (2.5 μ g/mL) for 2 h, washed with PBS, and treated with 200 μ L of different fluorescent agents (FITC-labeled INRs, RITC-labeled SOD, dual fluorescently labeled INRplex and Ab-INRplex) at FITC final concentration of 7.5 μ g/mL and RITC final concentration of 10 μ g/mL for 1, 2, 4 h. Lastly, the cells were fixed with 4% paraformaldehyde and stained with DAPI. For the study of the uptake mechanism, LPS-activated HUVECs were incubated with the endocytosis inhibitors: nystatin (10 μ mol/L), methyl β -cyclodextrin (M- β -CD, 2.5 mmol/L), chlorpromazine (CPZ, 10 μ g/mL), and nocodazole (20 μ mol/L) for 30 min before treatment with fluorescent Ab-INRplex for 4 h. The cells were tagged with Lyso-tracker Red to observe the endosomal entrapment.

2.9. Flow cytometry

For the quantitation of ICAM-1 expression on the surface of HUVECs, the cells were seeded in 12-well plates (8×10^5 cells/well) and incubated for 24 h at 37 °C. After activation with LPS (2.5 μ g/mL) for 2 h, the cells were incubated with ICAM-1 primary antibody (1:100) overnight at 4 °C, washed 3 times with PBS, treated with CoraLite 594 secondary antibodies (1:1000) at 37 °C for 1 h in the dark. Finally, the cells were trypsinized, centrifuged (300 \times g, TDZ5-WS, Cence®, Hunan Xiangyi Instrument Co., Ltd.), resuspended in PBS, and the fluorescence intensity was measured by flow cytometry (BD FACSCalibur, San Jose, CA, USA). Likewise, the LPS-activated HUVECs seeded in 12-well plates (8×10^5 cells/well) were treated with different fluorescent preparations for 1, 2, and 4 h to quantify their cellular uptake. Next, the treated LPS-activated HUVECs were digested, collected, centrifuged (300 \times g, TDZ5-WS, Cence®, Hunan

Xiangyi Instrument Co., Ltd.), resuspended in PBS, and assayed by flow cytometry. For the examination of the endocytic mechanism, the endocytosis inhibitors were added to the LPS-treated HUVECs for 30 min before treating the cells with fluorescent Ab-INRplex for 4 h.

2.10. SOD intracellular delivery efficiency and IND dissolution assay

HUVECs were seeded in 12-well culture plates (8×10^5 cells/well) and incubated for 24 h at 37 °C. After activation with LPS (2.5 µg/mL) for 2 h, the cells were treated with SOD, physical mixture, INRplex, and Ab-INRplex containing 100 µg/mL of SOD for 4 h. PBS and INR-treated cells were used as controls. Then, cells were detached and lysed in RIPA buffer. The total proteins were quantified by BCA assay kit (P0010, Beyotime Biotechnology, Shanghai, China). Finally, the SOD concentration in each group was determined using a specific ELISA kit. To test the IND dissolution after cellular uptake, we determined the intracellular drug concentration at 4, 12, and 24 h after incubation at 37 °C. The incubated cells were washed with PBS and harvested by trypsinization. Then, the cell pellets were lysed and centrifuged ($300 \times g$). The IND in the supernatant and the total internalized drug were assayed by the HPLC method.

2.11. In vitro evaluation of the anti-inflammatory effect

For the examination of inflammatory factors, HUVECs were seeded in 12-well culture plates (8×10^5 cells/well) and activated with LPS (2.5 µg/mL) for 2 h. Next, the cells were treated with IND, SOD, physical mixture, INRplex, and Ab-INRplex, containing 3.2 mg/mL of IND and/or 100 µg/mL of SOD for 4 h. Cells of each group were collected by trypsinization and lysed in RIPA. The intracellular levels of TNF- α , IL-6, and COX-2 were measured using specific ELISA kits.

2.12. In vitro evaluation of the antioxidant effect

The nonpolar dye DCFH-DA (2',7'-dichlorodihydrofluorescein diacetate) was used to assess the oxidative stress in HUVECs. For the study of the ROS-scavenging ability of SOD, cells were cultured onto 15-mm glass-bottom dishes at a density of 1×10^5 cells/well, incubated for 24 h at 37 °C, and stimulated with 2.5 µg/mL LPS for 2 h. Next, a serum-free medium containing 5 µmol/L DCFH-DA was added. After 30-min incubation in the dark at 37 °C, cells were washed with PBS, treated with preparations for 4 h containing 3.2 mg/mL of IND and/or 100 µg/mL of SOD, and imaged under CLSM. Similarly, HUVECs cultured in 12-well plates (8×10^5 cells/well) and activated with 2.5 µg/mL LPS for 2 h were incubated with DCFH-DA for 30 min at 37 °C, treated with the same concentrations of drugs for 4 h, and finally assayed by flow cytometry (BD FACSCalibur, San Jose, CA, USA).

2.13. Investigation of synergistic effect

HUVECs were cultured at a density of 8×10^5 in 12-well cell plates, stimulated with LPS (2.5 µg/mL) for 2 h, and treated with preparations containing different concentrations of SOD and IND for 4 h. The TNF- α expression in the cell lysates was measured by TNF- α ELISA Kit. Finally, the fraction affected (Fa) versus combination index (CI) plot was generated by CompuSyn software version 1.0 (ComboSyn, Inc., Paramus, NJ, USA).

2.14. Pharmacokinetics

The animals were randomly divided into two groups ($n = 5$). Free DiR and DiR-Ab-INRplex were injected into the tail vein at a DiR dose of 1.5 mg/kg. The orbital blood was taken at specific time points, and the blood samples were centrifuged ($1500 \times g$ for 5 min, TGL-16M, Cence, Hunan Xiangyi Instrument Co., Ltd.). Finally, the fluorescence intensity in each supernatant was measured using a multi-function microplate reader at the excitation/emission wavelength of 730/790 nm. The pharmacokinetic parameters were calculated by a non-compartmental model using Phoenix WinNonlin 8.1 (Certara, Princeton, NJ, USA).

2.15. Biodistribution study

The LPS-induced ALI mice were randomly divided into three groups ($n = 5$) and injected with free DiR, DiR-INRplex, and DiR-Ab-INRplex through the tail vein at a single DiR dose of 1.5 mg/kg. The animals were sacrificed at 4, 8, 12, and 24 h after injection. The major organs were dissected for *ex vivo* imaging (Ex: 768 nm; Em: 789 nm).

2.16. Pulmonary-endothelium targeting

The LPS-induced ALI mice were randomly divided into 3 groups ($n = 5$) and intravenously injected with free FITC, FITC-INRplex, and FITC-Ab-INRplex at a single FITC dose of 1 mg/kg. Mice were sacrificed at 4 h post-administration, and the lung tissues were dissected. Then, the lung sections were successively incubated with 5% BSA solution for 1 h at room temperature, ICAM-1 primary antibody (10 µg/mL) overnight at 4 °C, and CoraLite 594-labeled secondary antibodies (1:100) for 1 h at room temperature. Finally, the slides were visualized under a Leica upright fluorescence microscope (DM750, Wetzlar, Germany).

2.17. In vivo therapeutic efficiency

The animals were randomly divided into seven groups ($n = 5$), including saline (normal control), LPS (ALI model group), and the differently treated-ALI model groups, namely IND, SOD, physical mixture, INRplex, and Ab-INRplex, that received a single intravenous-injection dose of preparations containing 4.8 mg/kg of IND and/or 0.15 mg/kg of SOD. At 6 h after administration, the lung tissues were harvested, fixed in 4% paraformaldehyde, embedded in paraffin, and sliced into 5-µm sections. After deparaffinization and dehydration, the lung sections were stained with hematoxylin and eosin (H&E) for microscopic examination.

The lung tissue homogenates were prepared according to the ELISA kits manufacturer's instructions by homogenizing the tissue pieces in fresh lysis buffer ($w/v = 1 \text{ mg} : 50 \text{ mL}$) using a glass homogenizer on ice. The total protein concentration was determined by the BCA protein assay kit. The inflammatory factors were assessed using specific ELISA kits. ROS was measured using a ROS assay kit, and the optical density was calculated using a microplate reader (POLARstar, Omega, Germany) at 450 nm.

2.18. Statistical analysis

All results were presented as means \pm standard deviation (SD). All statistical analyses were performed using SPSS 10.0 software (IBM, Armonk, NY, USA). The difference between groups was assessed by one-way analysis of variance (ANOVA) or Student's *t*-

test when appropriate. P values < 0.05 were considered to be significant.

3. Results

3.1. Preparation and characterization of INRs, INRplex, and Ab-INRplex

Different amounts of IND and ultrasonication conditions were used to prepare the INRs using CLG as a stabilizer coating the nanoparticles. The smallest particle size was obtained with an ultrasonication of 400 W for 15 min and IND loading of 10 mg. The optimized INRs with rod shape had a hydrodynamic diameter of 160.5 ± 1.23 nm and a surface charge of approximately $+30 \pm 0.15$ mV (Supporting Information Fig. S1A–S1D). The interaction between IND and CLG was examined using fluorescence spectroscopy. As shown in Fig. S1E, the maximum fluorescence emission of CLG (λ_{\max}) was 340 nm, mainly attributed to its tryptophans' hydrophobic residues⁴⁹. The incorporation of IND in INRs led to a fluorescence quenching with a red shift of λ_{\max} from 340 to 490 nm, regardless of IND loading, indicating a strong interaction between CLG and IND. Remarkably, the fluorescence intensity increased when the IND loading was augmented from 5 to 20 mg due to the increased hydrophobic area of the INRs complex that further facilitated the protein adsorption. However, at high drug loadings (30–50 mg), the fluorescence signal did not intensify because the protein tended to adsorb on the hydrophobic surface of drug particles.

Also, CD spectroscopy was conducted to further understand the interaction between CLG and IND (Fig. S1F). CLG exhibited a typical spectrum with a broad minimum negative peak at 218 nm. Outstandingly, the IND loading influenced the CD spectrum of CLG. When the IND loading increased from 0 to 30 mg, the intensity of the positive peak at 190 nm was augmented, and the intensity of the negative peak at 208–225 nm diminished, with a blue shift of CLG at 208 nm (span of 1 to 2 nm). Moreover, PXRD was performed to confirm the crystallinity of INRs. As shown in Fig. S1G, IND exhibited several characteristic peaks between 3° and 40° . In contrast, no specific peaks were observed for CLG due to its amorphous physical state. The freeze-dried INRs displayed similar peaks as IND with no obvious different peaks indicating that IND preserved its crystalline state, although the peaks of INRs were not as intense as the raw powders, which may be attributed to the binding of CLG to IND.

Next, SOD was loaded onto the optimized INRs through electrostatic interaction to form INRplex. The gel electrophoresis demonstrated that the band disappeared as CLG:SOD mass ratio augmented from 1:1 to 64:1 (Supporting Information Fig. S2A), indicating the increased binding of SOD onto INRs, which was maximum when the ratios 32:1 and 64:1 were used. Alongside, the INRplex diameter slightly decreased, and the zeta potential increased due to the adsorption of the negatively charged SOD (Figs. S2B and S2C). The CLG/SOD mass ratio 32:1 was chosen to get a compromise between the SOD loading, INRplex size, and charge (170.8 ± 2.15 nm, $+20.3 \pm 0.53$ mV). Then, the attachment of anti-ICAM-1 antibody to INRplex was studied by changing the CLG:SOD:Ab mass ratio. The particle size of Ab-INRplex was proportionally augmented when the CLG:SOD:Ab mass ratio increased while the surface charge gradually decreased (Fig. 1A and B). The grafting efficacy of the anti-ICAM-1

antibody was affected by the feeding ratio (feed amount per 1 mg INRplex, Table S1). The greatest grafting efficacy (86.7%) was demonstrated in the ratio of 15. The Ab-INRplex with the ratio 32:1:1 was selected as the optimized formulation due to the highest grafting Ab-efficacy and the suitability of its size (237.0 ± 1.16 nm) for pulmonary accumulation.

The final preparation displayed a slightly milky color but was transparent and homogeneous in physical appearance. The encapsulation efficiency of IND and SOD in the optimized formulation was 64% and 76.8%, with drug loading of 39% and 2.3%, respectively. The TEM examination showed that INRs and Ab-INRplex had rod-like morphology with particle diameters of approximately 180 to 240 nm and with an aspect ratio of 6.5 (Fig. 1C and Fig. S1D). The size of Ab-INRplex at 37 °C didn't change significantly after 12-h incubation in serum (10% FBS) (Fig. 1D). Ab-INRplex released 69.4% and 61.9% of IND within 24 h at pH 6.8 and 7.4, respectively (Fig. 1E). Similarly, about 60% SOD was liberated from the codelivery system after 24 h with no significant difference as compared to IND, indicating the synchronous release of the two drugs (Fig. 1F). The measurement of the total SOD activity confirmed the maintained enzymatic activity during the *in vitro* release study (Supporting Information Fig. S3).

3.2. ICAM-1-targeting and enhanced intracellular delivery

First, an MTT assay was conducted to confirm the safety of INRs on HUVECs and PASCs (Supporting Information Fig. S4). The ICAM-1 expression on HUVECs was evaluated quantitatively and qualitatively. As depicted in Fig. 2A and B and Supporting Information Fig. S5, normal HUVECs expressed a low ICAM-1, whereas the expression was significantly upregulated after LPS activation. Afterward, LPS-stimulated HUVECs were used to evaluate the cellular uptake of naked SOD, INRplex, and Ab-INRplex. As shown in Fig. 2C, Ab-INRplex intensified the red fluorescence of SOD around the nuclei, indicating enhanced cytoplasmic delivery. Flow cytometry analysis displayed that Ab-INRplex increased the fluorescence by 40% compared to INRplex ($P < 0.01$, Fig. 2D), demonstrating the ICAM-1-targeting. Furthermore, the nanoparticle uptake was time-dependent in a 4-h period (Supporting Information Fig. S6). Interestingly, the internalized Ab-INRplex displayed sustained release of the small molecular drug in a 24-h period, releasing 19%, 28.5%, and 44.4% of total IND at 4, 12, and 24 h, respectively (Supporting Information Fig. S7). The data indicate that the IND nanocrystals could be solubilized after uptake. In addition, Ab-INRplex internalization could be mediated by caveolin/cholesterol-dependent pathways, as depicted by the weakened green and red fluorescence around the nucleus observed by CLSM after treatment with the endocytosis inhibitors, nystatin and M- β -CD (Supporting Information Fig. S8)⁴⁸. In contrast to the clathrin pathway that leads to the degradation of biological drugs in the acidic lysosomal compartment, the caveolin/cholesterol-mediated endocytosis avoids endo-lysosomal entrapment, thereby increasing the cytosolic delivery of drugs⁵⁰. The non-endo-lysosomal detainment was confirmed by the few yellow spots after merging the green fluorescence of preparation and the red fluorescence of endo-lysosomes (Supporting Information Fig. S9).

To demonstrate the intracellular delivery of SOD, we measured the protein level by ELISA. As indicated in Fig. 2E, the SOD level in INRplex- and Ab-INRplex-treated groups were remarkably higher, whereas the free SOD and the physical mixture didn't

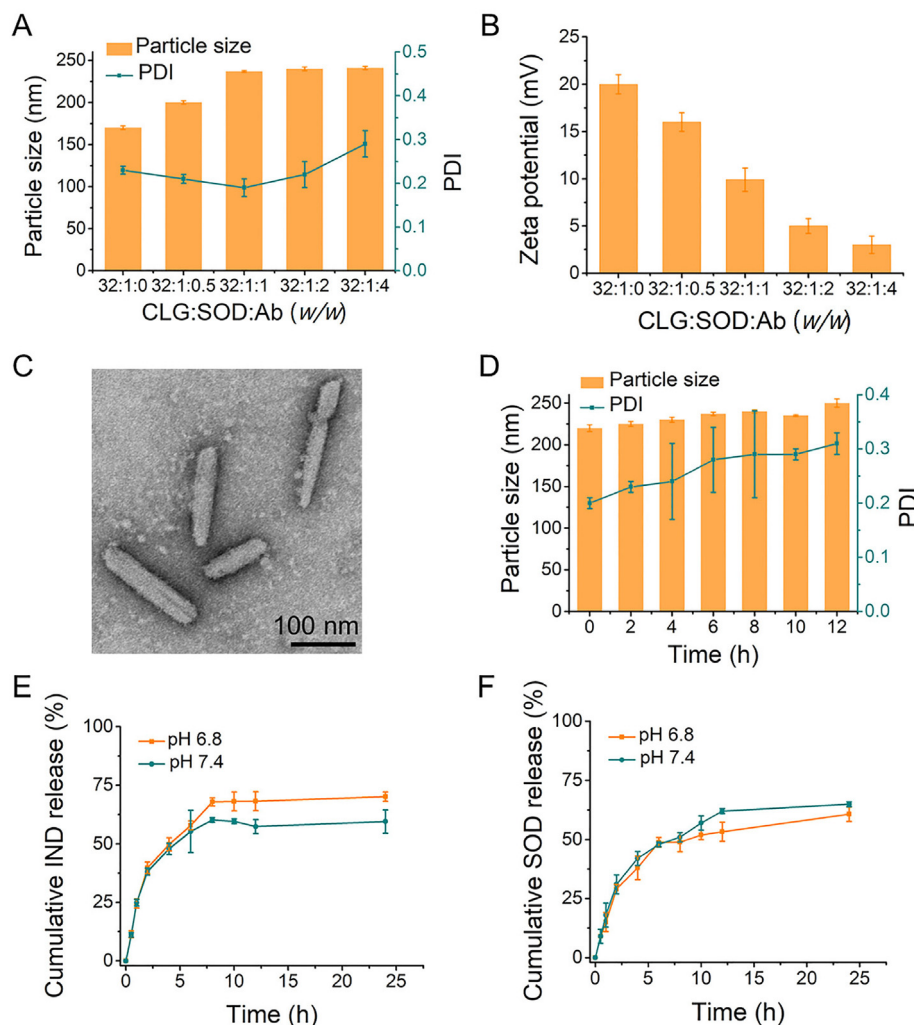


Figure 1 Preparation and characterization of Ab-INRplex. (A) The nanoparticles' particle size and (B) zeta potential with different CLG:SOD:Ab mass ratios. (C) TEM examination. Scale bar: 100 nm. (D) Serum (10%) stability at 37 °C. *In vitro* release of (E) IND and (F) SOD from Ab-INRplex at pH 7.4 and 6.8, $n = 3$.

increase the SOD level significantly compared to PBS- or INR-treated cells. These results indicated that Ab-INRplex could target LPS-activated HUVECs and improve intracellular delivery of SOD.

3.3. Efficient anti-inflammatory and antioxidant effects *in vitro*

We evaluated the anti-inflammatory and antioxidant effects of the preparations in LPS-induced HUVECs. The LPS activation allowed a 3-fold increase in IL-6, TNF- α , and COX-2 expression. Neither IND nor SOD treatment could significantly repress the production of IL-6 with limited TNF- α inhibition. However, INRplex and Ab-INRplex reduced the expression of IL-6 by 2 and 2.5-fold and TNF- α by 2.3- and 3-fold, respectively, compared to the LPS-induced positive control (Fig. 3A and B), indicating an efficient anti-inflammatory ability of the two preparations. IND lessens inflammation by inhibiting COX-2⁵¹. As shown in Fig. 3C, Ab-INRplex downregulated COX-2 with the highest efficacy among the IND-loaded preparations. Next, we investigated the antioxidant efficacy of preparations by ROS-scavenging ability

using the ROS-sensitive probe DCFH-DA^{52,53}. All SOD-containing preparations decreased green ROS fluorescence compared to the LPS-positive control, while weaker fluorescence was found in INRplex- and Ab-INRplex-treated groups (Fig. 3D). The quantitative analysis demonstrated that INRplex and Ab-INRplex downregulated ROS levels by 2.1- and 2.8-fold compared to the non-treated group; in contrast, the free SOD used alone or in combination with IND reduced ROS 1.5-fold (Fig. 3E). The data verified the robust ability of Ab-INRplex to relieve inflammation and oxidative stress in activated endothelial cells.

3.4. *In vitro* synergistic effect between IND and SOD

The TNF- α inhibition in LPS-activated HUVECs was used to study the synergy between the two drugs after treatment with IND, SOD, or Ab-INRplex. As expected, the inhibition rate of TNF- α in Ab-INRplex was significantly higher than IND or SOD used alone ($P < 0.001$) (Supporting Information Fig. S10A). As depicted in Fig. S10B, the combination index (CI) values of Ab-INRplex were lower than 1, with CI less than 0.5 for Fa = 0.2–0.90. CI < 1,

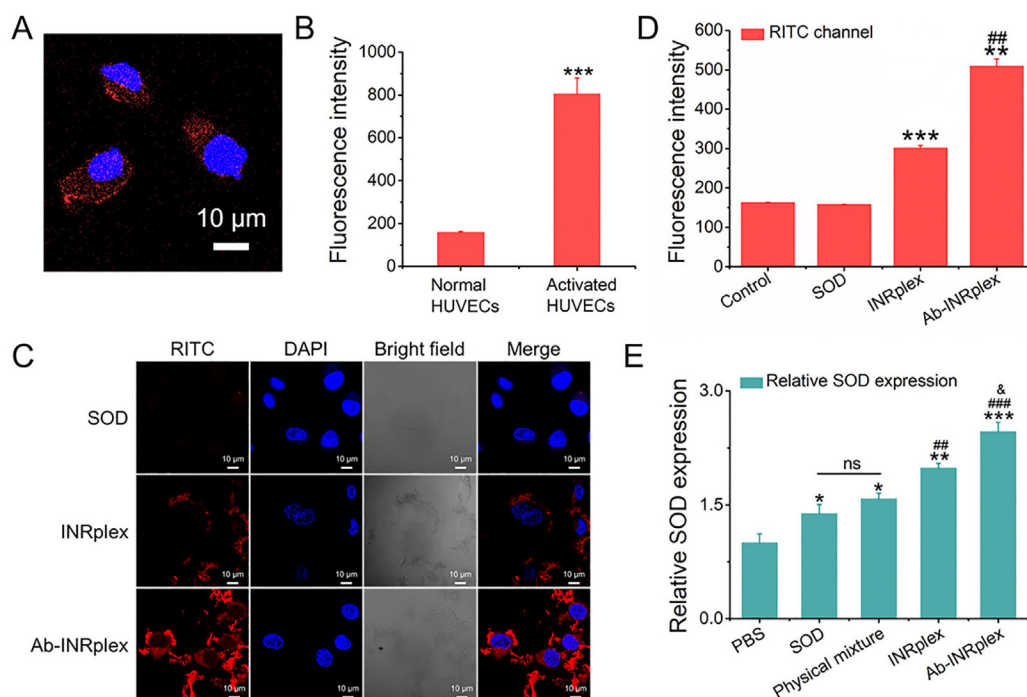


Figure 2 ICAM-1 expression and SOD intracellular delivery in LPS-activated HUVECs treated with different formulations. The ICAM-1 expression was evaluated qualitatively by (A) CLSM and quantitatively by (B) flow cytometry. The ICAM-1 was marked with CoraLite 594 labeled secondary antibody in red. ICAM-1 primary antibody and fluorescent secondary antibody dilution are 1:100 and 1:1000, respectively. $n = 3$, *** $P < 0.001$ compared to normal HUVECs. Cellular uptake of nanoparticles measured by (C) CLSM and (D) flow cytometry after incubation of LPS-induced HUVECs with RITC-labeled SOD, INRplex, and Ab-INRplex for 4 h at a RITC dose of 10 $\mu\text{g}/\text{mL}$. $n = 3$, ** $P < 0.01$, *** $P < 0.001$, compared to the control and SOD groups; ### $P < 0.01$, compared to INRplex group. Scale bar: 10 μm . (E) SOD expression in LPS-activated HUVECs determined by ELISA kit after incubation with different formulations containing 100 $\mu\text{g}/\text{mL}$ of SOD for 4 h. $n = 3$, * $P < 0.05$, ** $P < 0.01$, *** $P < 0.001$, compared with PBS; ## $P < 0.01$, ### $P < 0.001$, compared with SOD and physical mixture; & $P < 0.05$, compared to INRplex group; ns, not significant. Scale bar: 10 μm .

CI = 1, and CI > 1 indicate synergistic, additive, or antagonistic effects, respectively⁵⁴. Consequently, the data revealed a synergistic effect between the two drugs in Ab-INRplex.

3.5. Improved pharmacokinetics and prolonged blood circulation

The plasma concentrations of Ab-INRplex were assessed by detecting the fluorescence of DiR. The nanoparticles exhibited higher fluorescence intensity for 24 h than free DiR (Supporting Information Fig. S11). The pharmacokinetic behavior was greatly improved, as shown in Table 1. The blood half-life ($t_{1/2}$) of DiR-Ab-INRplex was extended by approximately 35-fold ($P < 0.001$), the area under the curve (AUC) increased by more than 17-fold ($P < 0.001$), and the clearance was reduced 15 times ($P < 0.05$), reflecting the prolonged blood circulation of the nanoparticles compared with the free DiR that was rapidly eliminated. The improved pharmacokinetics of Ab-INRplex could be ascribed to the Ab coating and rod-shaped structure. The Ab coating compromises the protein-corona-caused elimination; meanwhile, the rod-like particles could reduce phagocytosis by the reticuloendothelial system^{55,56}.

3.6. Enhanced lung accumulation and endothelium-targeting

For the investigation of lung accumulation, the nanoparticle biodistribution was studied by *ex vivo* imaging. As displayed in

Fig. 4A and B, there was no significant difference between the accumulation of free DiR and DiR-labeled nanoparticles (INRplex and Ab-INRplex) in the heart, spleen, and kidneys. Free DiR mainly accumulated in the liver, whereas the fluorescence intensities of DiR-nanoparticles were significantly higher in the lung. Besides, the pulmonary accumulation of DiR-nanoparticles increased over time (4–24 h), indicating their lung-targeting ability (Supporting Information Fig. S12). The lung-targeting of the nanoparticle is related to the particle shape³⁹. Rod-like particles larger than 100 nm were more internalized by endothelial cells, followed by their spherical, cylindrical, and cubic counterparts⁵⁷. Also, rod-like particles have shown enhanced tissue penetration and are prone to accumulate in the lung after intravenous injection^{44,58}. As expected, the pulmonary distribution of Ab-INRplex was greater than the non-targeted INRplex, which may be attributed to their anti-ICAM-1 moiety interacting with the overexpressed ICAM-1 on the pulmonary endothelium and the resulting enhanced attachment.

To investigate the pulmonary-endothelium targeting, we examined the nanoparticle accumulation at the pulmonary endothelium at 4 h after administration by studying the colocalization of FITC-labeled nanoparticles with the endothelial marker ICAM-1 under the upright fluorescence microscope and comparing it to free FITC and FITC-INRplex groups. As depicted in Fig. 5A, yellow fluorescence spots appeared after merging the fluorescence of FITC-labeled preparations (green) and ICAM-1 stained in red, demonstrating the targeting ability

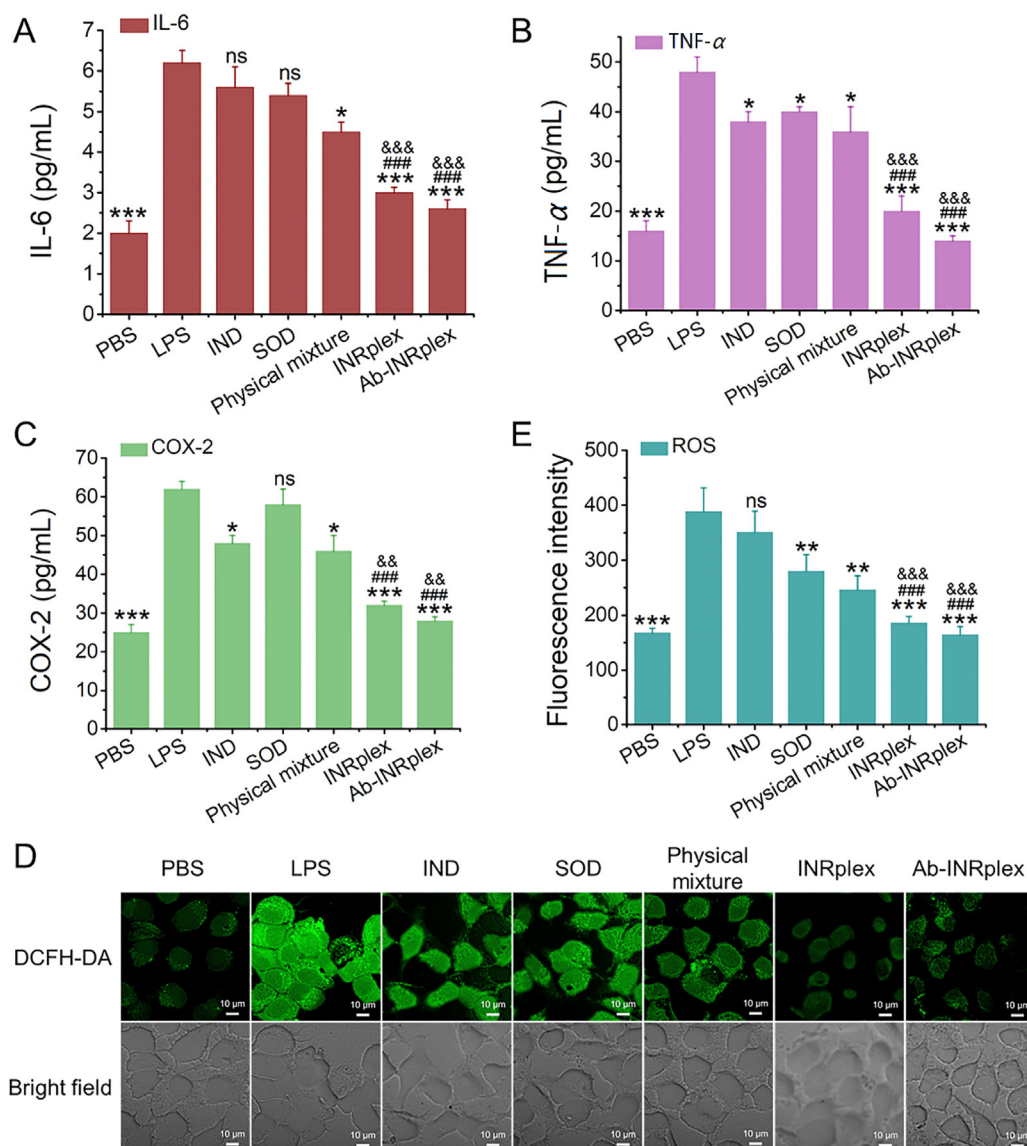


Figure 3 *In vitro* anti-inflammatory and anti-oxidant effects. (A) IL-6, (B) TNF- α , and (C) COX-2 expression measured by ELISA. (D) CLSM images of DCFH-DA probed LPS-activated HUVECs. (E) ROS expression assayed by flow cytometry. The HUVECs were activated with LPS (2.5 $\mu\text{g}/\text{mL}$) for 2 h before 4-h treatment with IND, SOD, IND/SOD, INRplex and Ab-INRplex containing 3.2 mg/mL of IND and/or 100 $\mu\text{g}/\text{mL}$ of SOD. The ROS-sensitive probe DCFH-DA was used to detect the intracellular ROS levels at a concentration of 5 μM . The data are expressed as mean \pm SD, $n = 5$; * $P < 0.05$, ** $P < 0.01$, *** $P < 0.001$, compared with the LPS group without treatment; # $P < 0.05$, ## $P < 0.01$, ### $P < 0.001$, compared with IND or SOD groups, && $P < 0.01$, &&& $P < 0.001$, compared with physical mixture group, ns, not significant. The PBS group is the normal HUVECs without LPS activation. The LPS group was the activated HUVECs treated with PBS. Scale bar: 10 μm .

of the nanoparticles. At the same time, the free FITC group displayed a weak green fluorescence and slight yellow fluorescence after merging channels. Remarkably, the difference between the FITC-Ab-INRplex and FITC-INRplex was significant ($P < 0.001$, Fig. 5B), confirming the enhanced targeting ability due to the anti-ICAM-1 coating. The data indicated that the nanoparticle shape and coating of the specific ligand Ab contributed to the endothelium targeting.

3.7. Alleviated pulmonary inflammation and oxidative stress in the ALI model

ALI represents a severe pulmonary inflammation disease with a high mortality rate. Herein, we used an LPS-induced model to

assess the anti-inflammation and antioxidant effects of the preparations. As shown in Fig. 6A, LPS stimulation significantly increased the alveolar wall thickness, alveoli congestion, and inflammatory cell infiltration. Consistently, the expression of the inflammatory and oxidative stress factors, TNF- α , IL-6, COX-2, and ROS, in the LPS model increased 1.5-fold compared to the normal group. The groups treated with the free drugs, IND, SOD, or their physical mixture didn't significantly differ from the LPS group. In contrast, INRplex and Ab-INRplex considerably inhibited inflammatory-cell infiltration and reduced the alveolar wall thickness (4- and 8-fold, respectively) compared to the LPS group (Fig. 6A and B). Moreover, the two nanosized preparations significantly lessened inflammation and relieved oxidative stress. Particularly, Ab-INRplex downregulated the expression of TNF- α ,

Table 1 Pharmacokinetic parameters of Ab-INRplex after intravenous injection ($n = 5$).

Formulation	$t_{1/2}$ (h)	AUC_{0-t} (mg·h/L)	$AUC_{0-\infty}$ (mg·h/L)	CL (mL/h/kg)	V_d (mL/kg)
Free DiR	0.33 ± 0.13	0.67 ± 0.09	1.50 ± 0.14	5.01 ± 0.79	78.13 ± 13.92
DiR-Ab-INRplex	11.53 ± 1.57***	11.45 ± 2.55***	14.70 ± 2.45***	0.34 ± 0.06*	5.91 ± 0.55**

AUC, the area under the curve; CL, the clearance rate; V_d , the apparent volume of distribution. The data are expressed as mean ± SD, $n = 5$; * $P < 0.05$, ** $P < 0.01$, *** $P < 0.001$ compared with the free DiR group.

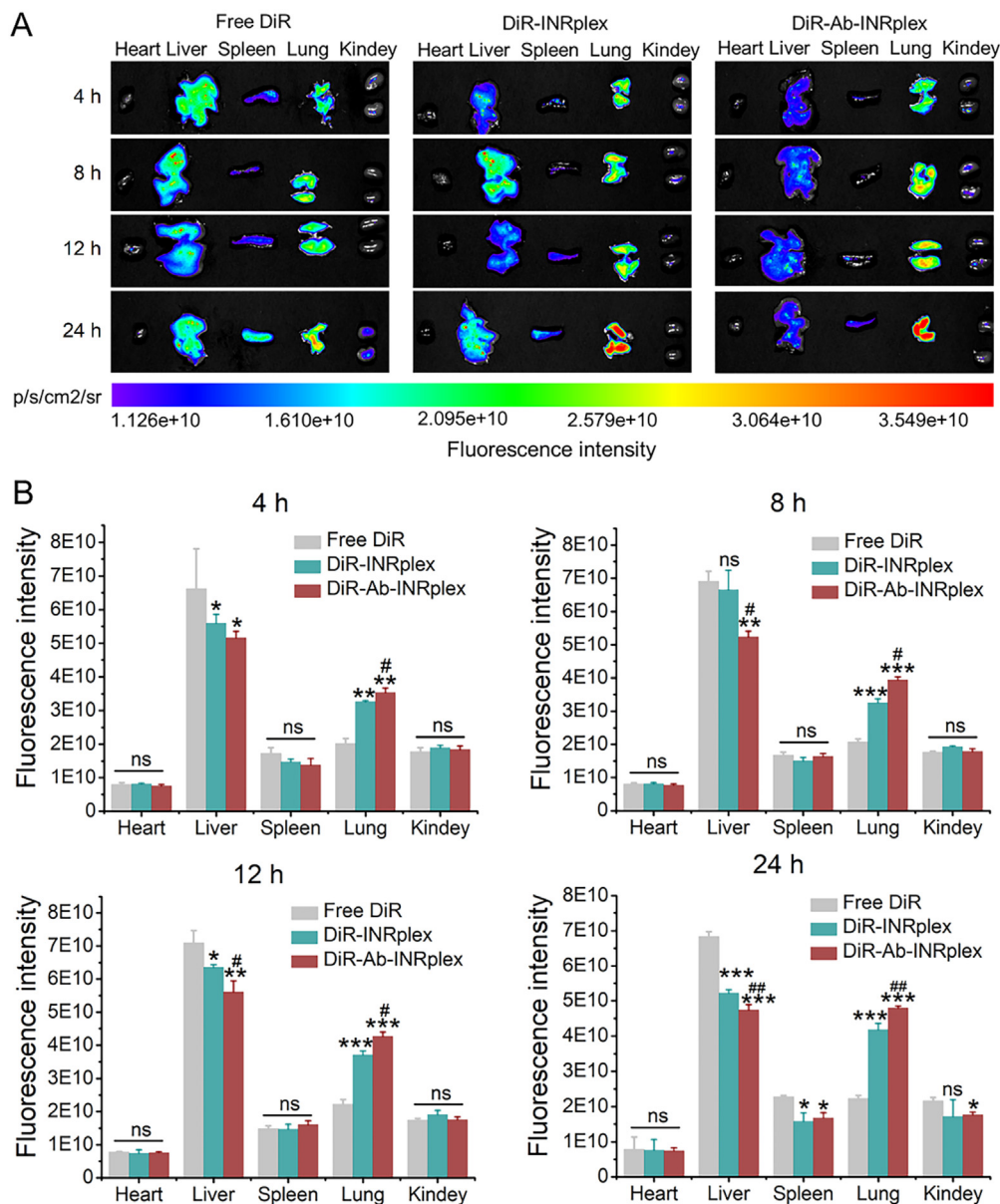


Figure 4 Biodistribution of DiR-labeled nanoparticles in LPS-induced ALI model. (A) Tissue distribution of DiR labeled nanoparticles at 4, 8, 12, and 24 h post-administration at a DiR dose of 1.5 mg/kg. (B) The semi-quantitative fluorescence intensity. The data are expressed as mean ± SD, $n = 3$, * $P < 0.05$, ** $P < 0.01$, *** $P < 0.001$, compared with free DiR; # $P < 0.05$, ## $P < 0.01$, compared with DiR-INRplex; ns, not significant.

IL-6, COX-2, and ROS by approximately 2-fold for TNF- α , 3-fold for IL-6, 1.5-fold for COX-2, and 1.4-fold for ROS compared with the physical mixture preparation (Fig. 6C–F). It is worth noting that Ab-INRplex exhibited an enhanced anti-inflammatory effect over INRplex, implying that pulmonary-endothelium targeting is essential for preparations to exert efficacy at a specific

administration dose. Additionally, its single intravenous injection did not cause additional inflammation in the normal lung, indicating its safety (Supporting Information Fig. S13). Collectively, the results demonstrated that INRplex and Ab-INRplex could effectively ameliorate pulmonary inflammation and oxidative stress in the lung inflammation model.

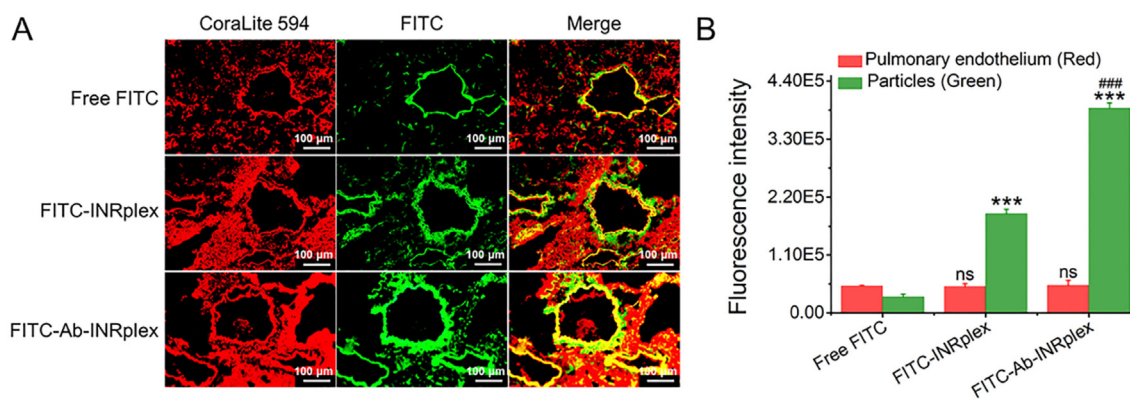


Figure 5 Pulmonary-endothelium targeting in LPS-induced ALI model. (A) Co-localization (yellow) of FITC-dyed Ab-INRplex (green) with the pulmonary-endothelium (red) stained with ICAM-1 primary antibody (10 µg/mL) and CoraLite 594 (1:100) secondary antibody. (B) The semi-quantitative analysis of the fluorescent images by “Image J” software. The data are expressed as mean ± SD, $n = 3$, *** $P < 0.001$, compared with free FITC; ### $P < 0.001$, compared with FITC-INRplex, ns, not significant. Scale bar: 100 µm.

4. Discussion

This study provided an effective pulmonary endothelium-targeted platform using rod-like drug crystals as a “vector”. Pulmonary endothelium injury and the resultant lung inflammation are vital drivers of various lung diseases such as ALI/ARDS, pulmonary hypertension, and thrombosis^{37,59,60}. Accordingly, pulmonary endothelium-targeted therapy against inflammation is increasingly attractive. To improve endothelium-targeting, scientists usually associate the endothelial-target ligands such as platelet/endothelial cell adhesion molecule 1 (PECAM-1), vascular cell adhesion molecule-1 (VCAM-1), and ICAM-1 antibodies with nanocarriers, including liposomes and lipid nanoparticles^{61–63}. Differing from the “soft” drug carriers with elastic deformation, we found that the “hard” rod-like drug crystal-based nanoparticles, INRplex and Ab-INRplex with a length diameter of 170–230 nm, efficiently targeted the pulmonary endothelium, along with enhanced targeting ability due to anti-ICAM-1 coating. Several factors contributed to the pulmonary-endothelium targeting of the developed nanoparticles. Elongated particles favor adhesion to the lung-microvascular vessels under flow situations due to an increase in surface area and the resultant shape-stimulated improvement of vascular attachment compared to sphere-shaped particles⁶⁴. Moreover, the elongated particles decreased phagocytosis and displayed prolonged circulation time^{55,56}. The pharmacokinetic results in Table 1 show that the nanoparticle blood half-life was extended 35-fold compared to the free dye, with a 13-fold decrease in the apparent volume of distribution (V_d). The data imply the nanoparticle phagocytosis by mononuclear cells and biodistribution was markedly compromised. A previous report also indicated that the rod-shaped drug crystals of insoluble drugs with a diameter of 160–500 nm in length were hardly internalized by cells⁴⁰. Additionally, we uncovered that the coating of anti-ICAM-1 antibodies increased the INRplex accumulation in the pulmonary endothelium by 1.5-fold, highlighting the importance of ligand modification for the targeting of rod-shaped particles. Unlike other rod-shaped particles prepared from inorganic or organic materials, the present nanoplatform based on rod-like drug crystals demonstrated high drug-loading capacity (41%, w/w) compared with the traditional carriers (3%–5%). Overall, the platform’s ability to target the pulmonary endothelium is mainly ascribed to the nanoparticle shape and the coating of anti-ICAM-

1. Our platform possesses promising potential against endothelium-associated diseases, such as ALI/ARDS, atherosclerosis, and pulmonary arterial hypertension.

Another finding of our study is that efficient codelivery of IND and SOD to target the pulmonary endothelium could significantly attenuate serious lung inflammation (ALI). Due to insufficient drugs reaching the injury site, the clinical ALI treatment is not always effective as expected. For example, the data in Fig. 6 revealed that the administration of free drugs or their combination allowed modest alleviation in lung inflammation. A recent report also indicated that free dexamethasone did not significantly ameliorate the lung inflammation response, whereas improved lung delivery of dexamethasone using nanoparticles relieved the inflammation with higher efficacy⁶⁵. Several reports stated that pulmonary-endothelium dysfunction is closely linked to lung inflammation diseases such as ALI and pulmonary hypertension^{37,59,60,66}. Here, we found that endothelium-targeted codelivery of IND and SOD using the nanoplatform effectively alleviated the inflammation and reduced the alveolar wall thickness in the LPS-induced ALI model. The enhanced anti-inflammation effect of the nanoparticles was predominantly ascribed to the improved intracellular trafficking, the synergy between IND and SOD, pulmonary endothelium-targeted codelivery, prolonged lung retention, etc. Even at 24 h post-injection, the INRplex and FITC-INRplex resided in the lung, probably owing to their caveolae-mediated endocytosis that facilitated endothelial endocytosis and tissue distribution^{67,68}. Similar to our previous studies, IND crystals allowed sustained drug dissolution and reduced elimination and metabolism, extending the retention time^{40,47,69}. The intracellular delivery pathway of nanoparticles is another crucial factor determining their efficiency. SOD, a protein drug, demonstrated robust potency against endothelial inflammation; however, its intracellular delivery is challenging due to high molecular weight, poor membrane penetration, and instability in the digestive endosomes/lysosomes^{70,71}. The study found that INRplex and Ab-INRplex could enter the cells *via* the caveolae pathway, avoiding the entrapment in the endo-lysosomal compartment, particularly for biologics prone to degradation in acidic environments⁴⁷. Noticeably, the intracellular drug crystals of poorly water-soluble drugs can maintain >7 h drug release compared to the traditional drug carriers releasing their cargos within several minutes due to lysosomal entrapment⁶⁹. Accordingly, the

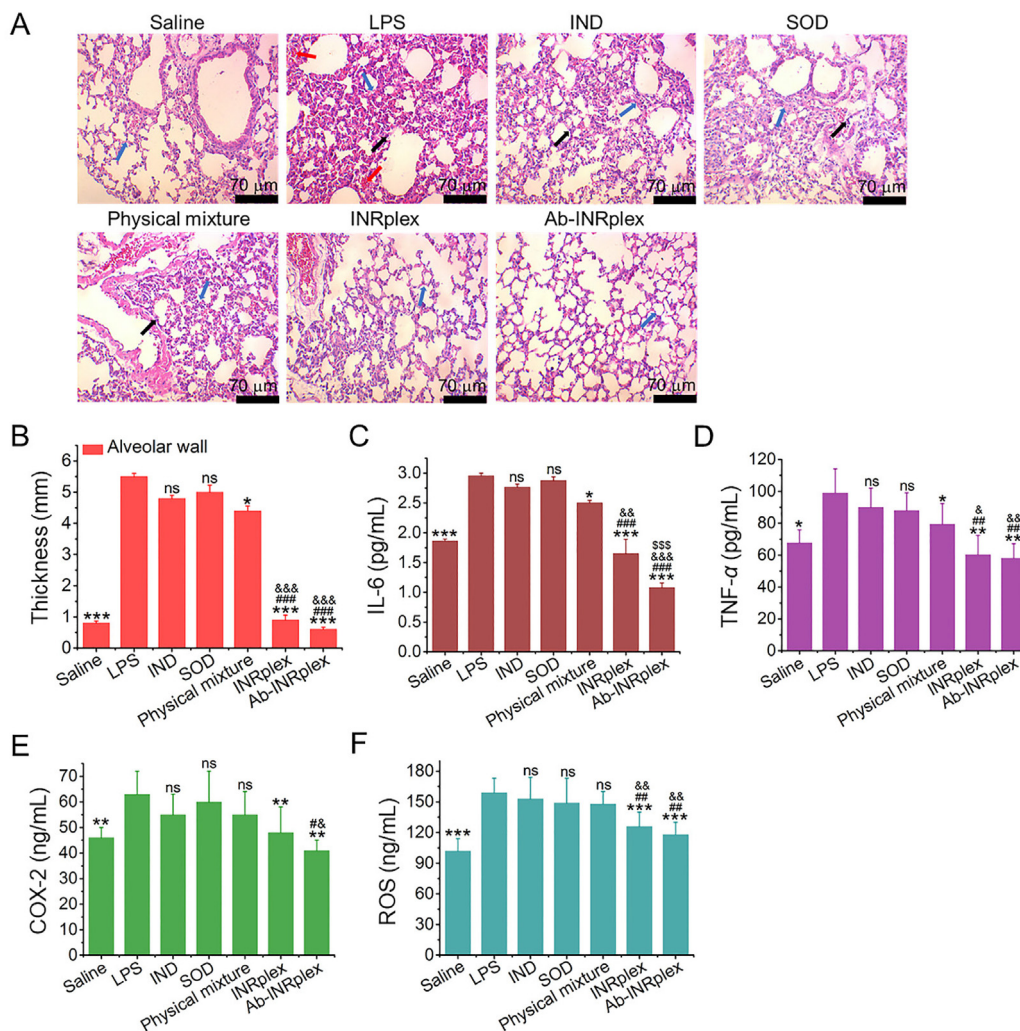


Figure 6 *In vivo* therapeutic efficiency in the LPS-induced ALI model. (A) Representative microscopy images of H&E-stained lung sections harvested at 6 h after a single intravenous injection. The blue, black, and red arrows indicate the alveolar wall, neutrophil infiltration, and alveolar congestion. (B) Semi-quantitative data of the alveolar wall thickness. (C) IL-6, (D) TNF- α , (E) COX-2, and (F) ROS expression. The dose of IND/SOD was 4.8/0.15 mg/kg, according to the body weight. The data are expressed as mean \pm SD, $n = 5$, * $P < 0.05$, ** $P < 0.01$, *** $P < 0.001$, compared with the LPS group; # $P < 0.05$, ## $P < 0.01$, ### $P < 0.001$, compared with IND or SOD groups; & $P < 0.05$, && $P < 0.01$, &&& $P < 0.001$, compared with physical mixture group; \$\$\$ $P < 0.001$, compared with INRplex group, ns, not significant. Scale bar: 70 μ m.

sustained drug release from the internalized nanoparticles may contribute to enhanced anti-inflammation and synergistic effects.

5. Conclusions

In this study, we developed a pulmonary endothelium-targeted codelivery system of the anti-inflammatory IND and antioxidant SOD, prepared by assembling SOD onto the rod-like pure IND crystals and having an extremely high drug-loading capacity. The targeted codelivery system allowed prolonged blood circulation, effective lung accumulation over time, and pulmonary endothelium-targeting with high efficacy. Moreover, the system could ameliorate the severe lung inflammation in the LPS-induced ALI model by downregulating the inflammatory/oxidative stress factors. Collectively, the present codelivery system can target the pulmonary endothelium and efficiently relieve lung inflammation. We provided a promising strategy to combat pulmonary endothelium-related diseases.

Acknowledgments

This study was supported by the National Natural Science Foundation of China, China (Nos. 81872823, 82073782 and 82241002), the Shanghai Science and Technology Committee, China (No. 19430741500), the Key Laboratory of Modern Chinese Medicine Preparation of Ministry of Education of Jiangxi University of Traditional Chinese Medicine, China (zdsys-202103).

Author contributions

Wei He and Zhenfeng Wu conceived and designed the research work. Wei He supervised the work. Yi Yang and Makhloufi Zoulikha carried out the experiments. Qingqing Xiao performed data analysis. Feifei Huang, Qi Jiang and Xiaotong Li participated part of the experiments. Makhloufi Zoulikha and Wei He wrote the manuscript. Makhloufi Zoulikha, Qingqing Xiao and Wei He

revised the manuscript. All of the authors have read and approved the final manuscript.

Conflicts of interest

The authors declare no conflicts of interest.

Appendix A. Supporting information

Supporting data to this article can be found online at <https://doi.org/10.1016/j.apsb.2023.05.024>.

References

- Van Eeden S, Leipsic J, Paul Man SF, Sin DD. The relationship between lung inflammation and cardiovascular disease. *Am J Respir Crit Care Med* 2012;**186**:11–6.
- Muhammad W, Zhu JQ, Zhai ZH, Xie JQ, Zhou JH, Feng XD, et al. ROS-responsive polymer nanoparticles with enhanced loading of dexamethasone effectively modulate the lung injury microenvironment. *Acta Biomater* 2022;**148**:258–70.
- Hao DL, Wang YJ, Yang JY, Xie R, Jia LY, Cheng JT, et al. The alleviation of LPS-induced murine acute lung injury by GSH-mediated PEGylated artesunate prodrugs. *Front Pharmacol* 2022;**13**:860492.
- Lian J, Lin JT, Zakaria N, Yahaya BH. Acute lung injury: disease modelling and the therapeutic potential of stem cells. *Adv Exp Med Biol* 2020;**1298**:149–66.
- Mokra D. Acute lung injury—from pathophysiology to treatment. *Physiol Res* 2020;**69**:S353–66.
- Qiao Q, Liu X, Yang T, Cui KX, Kong L, Yang CL, et al. Nano-medicine for acute respiratory distress syndrome: the latest application, targeting strategy, and rational design. *Acta Pharm Sin B* 2021;**11**:3060–91.
- Menk M, Estenssoro E, Sahetya SK, Neto AS, Sinha P, Slutsky AS, et al. Current and evolving standards of care for patients with ARDS. *Intensive Care Med* 2020;**46**:2157–67.
- Matthay MA, Zemans RL, Zimmerman GA, Arabi YM, Beitler JR, Mercat A, et al. Acute respiratory distress syndrome. *Nat Rev Dis Primers* 2019;**5**:19.
- Zoulikha M, Xiao QQ, Boafu GF, Sallam MA, Chen ZJ, He W. Pulmonary delivery of siRNA against acute lung injury/acute respiratory distress syndrome. *Acta Pharm Sin B* 2022;**12**:600–20.
- Orfanos SE, Mavrommati I, Korovesi I, Roussos C. Pulmonary endothelium in acute lung injury: from basic science to the critically ill. *Intensive Care Med* 2004;**30**:1702–14.
- Maniatis NA, Kotanidou A, Catravas JD, Orfanos SE. Endothelial pathomechanisms in acute lung injury. *Vascul Pharmacol* 2008;**49**:119–33.
- Huertas A, Guignabert C, Barberà JA, Bärtsch P, Bhattacharya J, Bhattacharya S, et al. Pulmonary vascular endothelium: the orchestra conductor in respiratory diseases. *Eur Respir J* 2018;**51**:17700745.
- Dai YJ, Ding YM, Li LL. Nanozymes for regulation of reactive oxygen species and disease therapy. *Chin Chem Lett* 2021;**32**:2715–28.
- Farella I, Panza R, Capozza M, Laforgia N. Lecithinized superoxide dismutase in the past and in the present: any role in the actual pandemic of COVID-19? *Biomed Pharmacother* 2021;**141**:111922.
- Rosa AC, Corsi D, Cavi N, Bruni N, Dosio F. Superoxide dismutase administration: a review of proposed human uses. *Molecules* 2021;**26**:1844.
- Huang XF, Xiu HQ, Zhang SF, Zhang GS. The role of macrophages in the pathogenesis of ALI/ARDS. *Mediators Inflamm* 2018;**2018**:1264913.
- Caruso AA, Del Prete A, Lazzarino AI. Hydrogen peroxide and viral infections: a literature review with research hypothesis definition in relation to the current COVID-19 pandemic. *Med Hypotheses* 2020;**144**:109910.
- Wu J. Tackle the free radicals damage in COVID-19. *Nitric Oxide* 2020;**102**:39–41.
- Qin M, Cao Z, Wen J, Yu QS, Liu CY, Wang F, et al. An antioxidant enzyme therapeutic for COVID-19. *Adv Mater* 2020;**32**:e2004901.
- Chow CW, Abreu MTH, Suzuki T, Downey GP. Oxidative stress and acute lung injury. *Am J Respir Cell Mol Biol* 2003;**29**:427–31.
- Robb CT, Goepf M, Rossi AG, Yao CC. Non-steroidal anti-inflammatory drugs, prostaglandins, and COVID-19. *Br J Pharmacol* 2020;**177**:4899–920.
- Nelin LD, Jin Y, Chen B, Liu YS, Rogers LK, Reese J. Cyclooxygenase-2 deficiency attenuates lipopolysaccharide-induced inflammation, apoptosis, and acute lung injury in adult mice. *Am J Physiol Regul Integr Comp Physiol* 2022;**322**:R126–35.
- Gye YP, Christman JW. Involvement of cyclooxygenase-2 and prostaglandins in the molecular pathogenesis of inflammatory lung diseases. *Am J Physiol Lung Cell Mol Physiol* 2006;**290**:L797–805.
- Meng FY, Gao W, Ju YN. Parecoxib reduced ventilation induced lung injury in acute respiratory distress syndrome. *BMC Pharmacol Toxicol* 2017;**18**:25.
- Ethridge RT, Chung DH, Slogoff M, Ehlers RA, Hellmich MR, Rajaraman S, et al. Cyclooxygenase-2 gene disruption attenuates the severity of acute pancreatitis and pancreatitis-associated lung injury. *Gastroenterology* 2002;**123**:1311–22.
- Shekhar N, Kaur H, Sarma P, Prakash A, Medhi B. Indomethacin: an exploratory study of antiviral mechanism and host-pathogen interaction in COVID-19. *Expert Rev Anti Infect Ther* 2022;**20**:383–90.
- Marinella MA. Indomethacin and resveratrol as potential treatment adjuncts for SARS-CoV-2/COVID-19. *Int J Clin Pract* 2020;**74**:e13535.
- Xu TH, Gao XJ, Wu ZB, Selinger DW, Zhou ZC. Indomethacin has a potent antiviral activity against SARS CoV-2 *in vitro* and canine coronavirus *in vivo*. *bioRxiv* 2020. Available from: <https://doi.org/10.1101/2020.04.01.017624>.
- Gomeni R, Xu TH, Gao XJ, Bressolle-Gomeni F. Model based approach for estimating the dosage regimen of indomethacin a potential antiviral treatment of patients infected with SARS CoV-2. *J Pharmacokinetic Pharmacodyn* 2020;**47**:189–98.
- Vaneev AN, Kost OA, Eremeev NL, Beznos OV, Alova AV, Gorelkin PV, et al. Superoxide dismutase 1 nanoparticles (Nano-SOD1) as a potential drug for the treatment of inflammatory eye diseases. *Biomedicines* 2021;**9**:396.
- Inada A, Oshima T, Takahashi H, Baba Y. Enhancement of water solubility of indomethacin by complexation with protein hydrolysate. *Int J Pharm* 2013;**453**:587–93.
- Altshuler PJ, Schiazza AR, Luo LJ, Helmers MR, Chhay B, Han JJ, et al. Superoxide dismutase-loaded nanoparticles attenuate myocardial ischemia-reperfusion injury and protect against chronic adverse ventricular remodeling. *Adv Ther* 2021;**4**:2100036.
- Younus H. Therapeutic potentials of superoxide dismutase. *Int J Health Sci (Qassim)* 2018;**12**:88–93.
- Zoulikha M, He W. Targeted drug delivery for chronic lymphocytic leukemia. *Pharm Res* 2022;**39**:441–61.
- Liu R, Luo C, Pang ZQ, Zhang JM, Ruan SB, Wu MY, et al. Advances of nanoparticles as drug delivery systems for disease diagnosis and treatment. *Chin Chem Lett* 2023;**34**:107518.
- Yang FJ, Ji QY, Liao R, Li SM, Wang YQ, Zhang XB, et al. Precisely engineering a dual-drug cooperative nanoassembly for proteasome inhibition-potentiated photodynamic therapy. *Chin Chem Lett* 2022;**33**:1927–32.
- Millar FR, Summers C, Griffiths MJ, Toshner MR, Proudfoot AG. The pulmonary endothelium in acute respiratory distress syndrome: insights and therapeutic opportunities. *Thorax* 2016;**71**:462–73.
- Cooley M, Sarode A, Hoore M, Fedosov DA, Mitragotri S, Sen Gupta A. Influence of particle size and shape on their margination and wall-adhesion: implications in drug delivery vehicle design across nano-to-micro scale. *Nanoscale* 2018;**10**:15350–64.
- Xiao QQ, Zoulikha M, Qiu M, Teng C, Lin CS, Li XT, et al. The effects of protein corona on *in vivo* fate of nanocarriers. *Adv Drug Deliv Rev* 2022;**186**:114356.

40. He W, Xin XF, Li YJ, Han XP, Qin C, Yin LF. Rod-shaped drug particles for cancer therapy: the importance of particle size and participation of caveolae pathway. *Part Part Syst Charact* 2017;**34**:1600371.
41. Lu Y, Lv YJ, Li TL. Hybrid drug nanocrystals. *Adv Drug Deliv Rev* 2019;**143**:115–33.
42. Magar KT, Boafu GF, Zoulikha M, Jiang XH, Li XT, Xiao QQ, et al. Metal phenolic network-stabilized nanocrystals of andrographolide to alleviate macrophage-mediated inflammation *in vitro*. *Chin Chem Lett* 2023;**34**:107453.
43. He W, Lu Y, Qi JP, Chen LY, Hu FQ, Wu W. Food proteins as novel nanosuspension stabilizers for poorly water-soluble drugs. *Int J Pharm* 2013;**441**:269–78.
44. Teng C, Li BB, Lin CS, Xing XY, Huang FF, Yang Y, et al. Targeted delivery of baicalein-p53 complex to smooth muscle cells reverses pulmonary hypertension. *J Control Release* 2022;**341**:591–604.
45. Guo MR, Wei MD, Li W, Guo MC, Guo CL, Ma MC, et al. Impacts of particle shapes on the oral delivery of drug nanocrystals: mucus permeation, transepithelial transport and bioavailability. *J Control Release* 2019;**307**:64–75.
46. Li BB, Teng C, Yu HL, Jiang XH, Xing XY, Jiang Q, et al. Alleviating experimental pulmonary hypertension *via* co-delivering FoxO1 stimulus and apoptosis activator to hyperproliferating pulmonary arteries. *Acta Pharm Sin B* 2022. Available from: <https://doi.org/10.1016/j.apsb.2022.12.002>.
47. Xin XF, Pei X, Yang X, Lv YQ, Zhang L, He W, et al. Rod-shaped active drug particles enable efficient and safe gene delivery. *Adv Sci* 2017;**4**:1700324.
48. Xin XF, Du XQ, Xiao QQ, Azevedo HS, He W. Drug nanorod-mediated intracellular delivery of microRNA-101 for self-sensitization *via* autophagy inhibition. *Nano-Micro Lett* 2019;**11**:82.
49. Li Y, Teng C, Azevedo HS, Yin LF, He W. Cocrystallization-like strategy for the codelivery of hydrophobic and hydrophilic drugs in a single carrier material formulation. *Chin Chem Lett* 2021;**32**:3071–5.
50. He W, Turkeshi A, Li XT, Zhang HW. Progress in systemic codelivery of microRNAs and chemotherapeutics for cancer treatment by using lipid-based nanoparticles. *Ther Deliv* 2020;**11**:591–603.
51. Abdellatif KRA, Abdelall EKA, Elshemy HAH, El-Nahass ES, Abdelfattah MM, Abdelgawad YYM. New indomethacin analogs as selective COX-2 inhibitors: synthesis, COX-1/2 inhibitory activity, anti-inflammatory, ulcerogenicity, histopathological, and docking studies. *Arch Pharm (Weinheim)* 2021;**354**:e2000328.
52. Yang RL, Li YQ, Wang XY, Yan JJ, Pan DH, Xu YP, et al. Doxorubicin loaded ferritin nanoparticles for ferroptosis enhanced targeted killing of cancer cells. *RSC Adv* 2019;**9**:28548–53.
53. Akhtar MJ, Ahamed M, Alhadlaq HA, Alshamsan A. Mechanism of ROS scavenging and antioxidant signalling by redox metallic and fullerene nanomaterials: potential implications in ROS associated degenerative disorders. *Biochim Biophys Acta Gen Subj* 2017;**1861**:802–13.
54. Xiao QQ, Li XT, Liu C, Jiang YX, He YL, Zhang WT, et al. Improving cancer immunotherapy *via* co-delivering checkpoint blockade and thrombospondin-1 downregulator. *Acta Pharm Sin B* 2022. Available from: <https://doi.org/10.1016/j.apsb.2022.07.012>.
55. Hadji H, Bouchemal K. Advances in the treatment of inflammatory bowel disease: focus on polysaccharide nanoparticulate drug delivery systems. *Adv Drug Deliv Rev* 2022;**181**:14101.
56. Champion JA, Mitragotri S. Shape induced inhibition of phagocytosis of polymer particles. *Pharm Res* 2009;**26**:244–9.
57. Nong J, Glassman PM, Muzykantor VR. Targeting vascular inflammation through emerging methods and drug carriers. *Adv Drug Deliv Rev* 2022;**184**:114180.
58. Da Silva-Candal A, Brown T, Krishnan V, Lopez-Loureiro I, Ávila-Gómez P, Pusuluri A, et al. Shape effect in active targeting of nanoparticles to inflamed cerebral endothelium under static and flow conditions. *J Control Release* 2019;**309**:94–105.
59. Evans CE, Cober ND, Dai ZY, Stewart DJ, Zhao YY. Endothelial cells in the pathogenesis of pulmonary arterial hypertension. *Eur Respir J* 2021;**58**:2003957.
60. Ding BS, Zhou YJ, Chen XY, Zhang J, Zhang PX, Sun ZY, et al. Lung endothelium targeting for pulmonary embolism thrombolysis. *Circulation* 2003;**108**:2892–8.
61. Howard MD, Greineder CF, Hood ED, Muzykantor VR. Endothelial targeting of liposomes encapsulating SOD/catalase mimetic EUK-134 alleviates acute pulmonary inflammation. *J Control Release* 2014;**177**:34–41.
62. Abd Elwakil MM, Khalil IA, Elewa YHA, Kusumoto K, Sato Y, Shobaki N, et al. Lung-endothelium-targeted nanoparticles based on a pH-sensitive lipid and the GALA peptide enable robust gene silencing and the regression of metastatic lung cancer. *Adv Funct Mater* 2019;**29**:1970121.
63. Glassman PM, Myerson JW, Ferguson LT, Kiseleva RY, Shuvaev VV, Brenner JS, et al. Targeting drug delivery in the vascular system: focus on endothelium. *Adv Drug Deliv Rev* 2020;**157**:96–117.
64. Kolhar P, Anselmo AC, Gupta V, Pant K, Prabhakarandian B, Ruoslahti E, et al. Using shape effects to target antibody-coated nanoparticles to lung and brain endothelium. *Proc Natl Acad Sci U S A* 2013;**110**:10753–8.
65. García-Fernández A, Sancho M, Bisbal V, Amorós P, Marcos MD, Orzáez M, et al. Targeted-lung delivery of dexamethasone using gated mesoporous silica nanoparticles. A new therapeutic approach for acute lung injury treatment. *J Control Release* 2021;**337**:14–26.
66. Jiang JY, Huang K, Xu SQ, Garcia JGN, Wang C, Cai H. Targeting NOX4 alleviates sepsis-induced acute lung injury *via* attenuation of redox-sensitive activation of CaMKII/ERK1/2/MLCK and endothelial cell barrier dysfunction. *Redox Biol* 2020;**36**:101638.
67. Okamoto CT. Endocytosis and transcytosis. *Adv Drug Deliv Rev* 1998;**29**:215–28.
68. Pelkmans L, Helenius A. Endocytosis *via* caveolae. *Traffic* 2002;**3**:311–20.
69. Teng C, Lin CS, Huang FF, Xing XY, Chen SY, Ye L, et al. Intracellular codelivery of anti-inflammatory drug and anti-miR 155 to treat inflammatory disease. *Acta Pharm Sin B* 2020;**10**:1521–33.
70. Shuvaev VV, Han JY, Tliba S, Arguiri E, Christofidou-Solomidou M, Ramirez SH, et al. Anti-inflammatory effect of targeted delivery of SOD to endothelium: mechanism, synergism with NO donors and protective effects *in vitro* and *in vivo*. *PLoS One* 2013;**8**:e77002.
71. He W, Xing XY, Wang XL, Wu D, Wu W, Guo J, et al. Nanocarrier-mediated cytosolic delivery of biopharmaceuticals. *Adv Funct Mater* 2020;**30**:1910566.